ACS APPLIED MATERIALS & INTERFACES

Research Article

www.acsami.org

Mitochondria-Targeting Nanoplatform with Fluorescent Carbon Dots for Long Time Imaging and Magnetic Field-Enhanced Cellular Uptake

Ye Zhang,[†] Yajing Shen,[†] Xiyao Teng,[†] Manqing Yan,[†] Hong Bi,*[,†,‡] and Paulo Cesar Morais[§,⊥]

[†]College of Chemistry and Chemical Engineering, Anhui University, Hefei 230601, China

[‡]Institute of Health Sciences, Anhui University, Hefei 230601, China

[§]School of Automation, Huazhong University of Science Technology, Wuhan 430074, China

[⊥]Instituto de Física, Universidade de Brasília, Brasília, Federal District 70910-900, Brazil

Supporting Information

ABSTRACT: In this study, a biocompatible nanoplatform has been constructed on the basis of magnetic mesoporous silica nanoparticles (Fe_3O_4@$mSiO_2$) via surface modification of triphenylphospine (TPP) and then conjugation with fluorescent carbon dots (CDs). The as-prepared Fe_3O_4@$mSiO_2$−TPP/CDs nanoplatform shows a very low cytotoxicity and apoptosis rate in various cell lines such as A549, CHO, HeLa, SH-SY5Y, HFF, and HMEC-1. More importantly, this nanoplatform integrates long time cell imaging, mitochondria-targeting, and magnetic field-enhanced cellular uptake functionalities into an all-in-one system. Time-dependent mitochondrial colocalization in all of the cell lines has been proved by using confocal laser scanning microscopy and flow cytometry, while the multicolored fluorescence of the Fe_3O_4@$mSiO_2$−TPP/CDs could remain bright and stable after coincubation for 24 h. In addition, the cellular uptake efficiency could be enhanced in a short time as a static magnetic field of 0.30 T was applied to the coincubation system of A549 and HFF cell lines. This bionanoplatform may have potential applications in targeted drug delivery for mitochondria diseases as well as early cancer diagnosis and treatment.

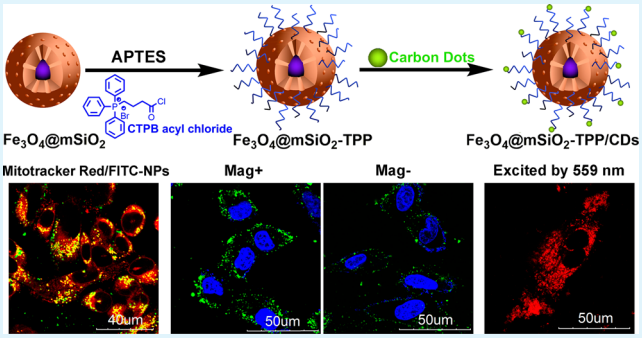

KEYWORDS: *mitochondrial targeting, carbon dots, magnetic field, cellular uptake, bioimaging, nanoplatform*

INTRODUCTION

The development of therapeutic approaches for cancer treatment demanding higher efficacy has fostered the engineering of multifunctional nanosystems. A biocompatible multifunctional nanosystem, usually called a bionanoplatform, aims to construct new approaches to integrate cancer treatment, imaging, and drug delivery functionalities in an all-in-one system.[1,2] In the evolution of bionanoplatforms engineering, superparamagnetic Fe_3O_4 nanoparticles (NPs) are probably one of the most appealing candidates, given the success of T_2 as a contrast agent for magnetic resonance imaging (MRI), as well as superparamagnetism for magnetic-targeted drug delivery and magnetohyperthermia (MHT) therapy.[3,4] Conjugated with fluorescent quantum dots or photosensitive reagents, the Fe_3O_4 NPs-based bionanoplatform can combine a dual imaging probe for cancer[5] with magnetically guided drug delivery,[6] targeted chemotherapy,[7] or photodynamic therapy (PDT),[8] and photothermal therapy.[9] In the past decades, mesoporous silica nanoparticles (MSNs) are known to have little or no toxicity due to favorable biocompatibility of silicon. Moreover, surface modified or end-capped MSNs are excellent nanopalt-forms for targeting drug delivery and chemotherapy, owing to their distinctive mesoporous structure, large surface area, tunable pore size, facile functionalization chemistry, and good biocompatibility.[10−12] Particularly, the engineered design of a mesoporous silica shell on a magnetite nanocrystal core (Fe_3O_4@$mSiO_2$) endows the as-constructed nanoplatform with multifunctionalities including MRI, fluorescence imaging, and magnetic targeted-drug delivery.[13] In addition, magnetic NPs under an applied magnetic field could direct cancer-targeting drug delivery,[14] enhance T cell activation so as to stimulate antitumor activity,[15] promote cell sorting,[16] and modulate cellular uptake.[17] Though the mechanism and exact process of magnetic NPs cellular uptake assisted by an applied magnetic field is still unclear, most of the research regarding the multifunctional Fe_3O_4@$mSiO_2$ NPs has focused on combining drug delivery system (DDS) with biosensing[18] or MRI functionalities.[19]

Recently, advances in biomedical nanotechnology make subcellular-targeted therapy an emerging important area for cancer treatment. Compared to the random interaction of drugs with intracellular site of action, the therapeutic outcomes

Received: January 14, 2015
Accepted: April 27, 2015
Published: May 5, 2015

DOI: 10.1021/acsami.5b00405
ACS Appl. Mater. Interfaces 2015, 7, 10201−10212

could be enhanced manyfold if pharmaceutical agents can be specifically directed toward the targeted organelle, i.e., pro-apoptotic compounds to mitochondria.[20,21] In general, the advantages of organelle targeting construction in chemotherapy are to achieve a higher drug efficacy as well as a minimum side effect. The mitochondrion is a double-membrane of phospholipid bilayer enveloped cytoplasmic organelle that possesses its own internal genome. The mitochondria are indispensable for providing energy for the survival of eukaryotic cells and to control the activation of programmed cell death (so-called apoptosis) mechanism by regulating the translocation of pro-apoptotic proteins from the mitochondrial intermembrane space to the cytosol.[22] Therefore, the mitochondrion is recognized as an important therapeutic target in cancer therapy, and many researchers have attempted to design mitochondria-targeted pharmaceuticals and drug carriers.[23−25] Triphenylphosphonium (TPP) is a representative lipophilic cationic species that can selectively accumulate in the mitochondria by reducing the free energy change while moving from an aqueous to the hydrophobic environment in response to the mitochondrial membrane potential of about −180 to −200 mV.[26] Through conjugation with TPP, several biologically active molecules, such as coenzyme Q or vitamin E derivative, have been selectively targeted to mitochondria to enhance antioxidant efficacy.[27,28] In recent years, various kinds of mitochondria-targeted TPP-conjugated nanosystems have been developed, including liposomes,[29] dendrimers,[30] polymeric nanoparticles[31−34] and small molecules.[35] Compared to the nontargeted counterparts, a TPP-conjugated nanosystem shows a remarkable improvement in the drug therapeutic index for cancer, Alzheimer's disease, and obesity.[31]

From last century, organic dyes and fluorescent proteins have been widely used in many biomedical fields, but their poor photobleaching property is not suitable for long-term and real-time bioimaging. Fluorescent quantum dots (QDs) are newly appealing high quality bioprobes for applications in diverse biological research because of their size-tunable emission, strong fluorescence, and high photostability.[36] However, fluorescent II/VI semiconductor QDs, one kind of the well-studied QDs, are handicapped by a potential toxicity problem due to release of heavy metal ions (e.g., Cd ions).[37] To overcome these limits in biomedical applications, biocompatible QDs, i.e., carbon QDs,[38] silicon QDs,[39] and novel nitrogen-rich QDs,[40] have attracted more and more attention and being continuously studied. Among them, carbon quantum dots (CDs), as a new carbon material of less than 10 nm in size,[41] have been receiving growing research interest since they were discovered in 2004.[42] CDs possess many advantages, such as ease of production, high fluorescent activity, resistance to photobleaching, and excellent biocompatibility, make them very promising for long time bioimaging.[43,44] Furthermore, it is postulated that the doping of nitrogen atoms can introduce the CDs a new kind of surface state, and their quantum yields are greatly elevated. Nitrogen and sulfur codoped CDs have been synthesized from a precursor comprising L-cysteine and citric acid, showing high yield and excitation-independent emission.[45] Recently, the one-pot hydrothermal synthesis of nitrogen-doped CDs (NCDs) from different nitrogen sources has been reported, and the obtained NCDs emit bright blue fluorescence. Cellular toxicity test and bioimaging experiment have demonstrated that NCDs not only possess low toxicity to cells but also have stronger resistance to photobleaching than CDs and thus have better performance in labeling than CDs.[46] Previously, NCDs in size of 2−3 nm with a high quantum yield (22% in ethanol) as well as low cytotoxicity have been synthesized and employed for live cell imaging in our lab.[47] In this paper, the as-synthesized CDs were conjugated with TPP-modified Fe_3O_4@$mSiO_2$ to construct a novel biocompatible nanoplatform (Fe_3O_4@$mSiO_2$−TPP/CDs) for mitochondria-targeting, long time cell imaging, and magnetic field-enhanced cellular uptake.

MATERIALS AND METHODS

Materials. Ferrous ammonium sulfate ($FeSO_4{\cdot}(NH_4)_2SO_4{\cdot}6H_2O$), sodium hydroxide (NaOH), oleic acid, cetyltrimethylammonium bromide (CTAB), tetraethyl orthosilicate (TEOS), ethyl acetate (EtOAc), ammounium nitrate (NH_4NO_3), TPP, α-bromobutyric acid, thionyl chloride, *n*-hexane, chloroform, ethanol, ethylenediaminetetraacetic acid (EDTA), and dimethyl sulfoxide (DMSO) were purchased from Sinopharm Chemical Reagent Co. and used without further purification. Dimethylformamide (DMF) and toluene were obtained from Sinopharm Chemical Reagent Co. and distilled under reduced pressure before use. Albumin from bovine serum (BSA) was purchased from Aladdin Industrial Corporation. 3-Aminopropyltriethoxysilane (APTES), fluorescein isothiocyanate (FITC) and 3-(4,5-dimethylthiazol-2-yl)-2,5-diphenyltetrazolium bromide (MTT) were purchased from Sigma-Aldrich Chemicals and used as received. The food-grade konjac flour (KF, 50 wt %) was donated from Biosharp Co. USA. Dulbecco's modified Eagle's medium (DMEM), penicillin/streptomycin, and fetal bovine serum (FBS) were purchased from Hyclone. The LDH assay kit was supplied by Nanjing Jian Chen BioChem Co. MCDB 131 medium, microvascular growth supplement (MVGS), Mitotracker Red, and Lysotracker Red DND-99 were obtained from Invitrogen. Hoechst 33258 and 4′,6-diamidino-2-phenylindole (DAPI) were supplied by Beyotime Institute of Biotechnology. Ultrapure water was used throughout for all experiments.

Synthesis of Fe_3O_4@$mSiO_2$. First, uniform magnetite NPs were prepared according to a typical liquid−solid−solid synthetic route as follows.[48] The Fe^{2+}-rich suspension was obtained by adding the $FeSO_4{\cdot}(NH_4)_2SO_4{\cdot}6H_2O$ aqueous solution (0.15 M) into a mixture comprising NaOH (2.0 g), oleic acid (20 mL), and ethanol (20 mL) followed by stirring at room temperature for a period of time. Second, the prepared suspension was transferred to a 100 mL Teflon-lined autoclave and maintained at 180 °C for 10 h. The product was extracted with *n*-hexane and ethanol and further purified by magnetic separation and washing with ethanol several times. Third, the obtained oleic acid-capped Fe_3O_4 NPs were dispersed in *n*-hexane again, and then they were transferred from *n*-hexane to water in a typical procedure by adding CTAB aqueous solution (0.55 M).[49] The Fe_3O_4/CTAB aqueous solution was diluted into certain amount of water and the temperature of the solution was kept at 60 °C. The NaOH solution (2 M) was added to adjust the pH value to 12 and appropriate amounts of TEOS and EtOAc were slowly added into the reaction medium in sequence. After speedy-stirring for 30 s, the suspension was aged for 3 h. The Fe_3O_4@$mSiO_2$ NPs were collected by centrifugation and washed with ethanol three times. To remove the excess of CTAB from the product, the Fe_3O_4@$mSiO_2$ NPs were dispersed into 10 mg/mL of NH_4NO_3/ethanol solution and refluxed twice at 80 °C for 3 h.

Synthesis of Fe_3O_4@$mSiO_2$−TPP. As shown in Scheme S1 of Supporting Information, at the beginning, amino-modified NPs (Fe_3O_4@$mSiO_2$−NH_2) were prepared by suspending 0.10 g of the Fe_3O_4@$mSiO_2$ NPs in a round-bottom flask with 1 mL of APTES and 50 mL of toluene and then refluxing for 24 h. The Fe_3O_4@$mSiO_2$−NH_2 was then collected by centrifugation, washed with toluene and ethanol, and dried under vacuum at 60 °C. Subsequently, (carboxyethyl)triphenylphosphonium bromide (CTPB) was obtained as follows. 2.63 g of TPP was dissolved into 30 mL of toluene and heated up to 40 °C. Once the temperature of the medium reached 40 °C, 0.20 g of α-bromobutyric acid was quickly added and the suspension was heated up to 120 °C. The reaction medium was kept under stirring at 120 °C for 4 h, after which the product was collected by filtration, washed with diethyl ether several times, and dried under

DOI: 10.1021/acsami.5b00405
ACS Appl. Mater. Interfaces 2015, 7, 10201−10212

vacuum at 40 °C. Finally, 0.20 g of the Fe_3O_4@$mSiO_2$−NH_2 NPs were dissolved into 20 mL of DMF under stirring and heated up to 60 °C. And then 0.10 g of CTPB and 0.50 mL of thionyl chloride were added into the DMF-based suspension, and the solutions was kept under stirring at 60 °C for 12 h. The suspension was centrifuged and the final product comprising Fe_3O_4@$mSiO_2$−TPP was washed with ethanol three times and dried under vacuum at 60 °C.

Construction of the Fe_3O_4@$mSiO_2$−TPP/CDs nanoplatform. CDs were obtained from pyrolysis of konjac flour (KF) under air atmosphere at 470 °C for 1.5 h as previously reported.[56] Then, 2 mg of the Fe_3O_4@$mSiO_2$−TPP NPs were dispersed in ethanol and 0.50 mg of the as-prepared fluorescent CDs was added. After ultrasonication for 30 min, the mixture was stored overnight. Finally, the Fe_3O_4@$mSiO_2$−TPP/CDs nanoplatform was collected by centrifugation and washed with ethanol three times to remove the excess of CDs.

Morphology and Structure Characterization. The morphology of the samples was observed by using transmission electron microscopy (200 kV JEM-2100 TEM, JEOL Ltd. Japan). X-ray diffraction (XRD) and small-angle X-ray diffraction (SAXD) patterns were recorded using an X'Pert PRO diffractometer equipped with a Cu Kα radiation source. The room temperature magnetic property of the products were assessed by a physics property measurement system (PPMS EC-II, Quantum Design). The specific surface area of samples were obtained based on an N_2 adsorption−desorption isothermal analysis (V-Sorb 2800P, Gold APP Instruments) with the Brunauer−Emmett−Teller (BET) model whereas the Barret−Joyner−Halenda (BJH) method was used to calculate the pore size. Thermal gravimetric analysis (TGA) was performed on an SDT Q600 instrument by heating the sample up to 800 °C at a constant rate of 10 °C/min under N_2 atmosphere. The ζ-potentials of the samples were measured using a Nano Zeta Potential Analyzer (Delsa 440SX Beckman Coulter Limited, USA). The hydrodynamic diameters were measured by a Malvern Zetasizer Nano ZS90 analyzer (Worcestershire, UK). The photoluminescence (PL) measurements and the ^1H NMR spectra were recorded using a Hitachi F-4500 fluorescence spectrophotometer and a 400 MHz Bruker NMR spectrometer, respectively.

Cell Culture. A549 (Human pulmonary adenocarcinoma cells), CHO (Chinese hamster ovary cell line), HeLa (Human cervical cancer cell), SH-SY5Y (Human neuroblastoma), and HFF (Human foreskin fibroblast cell) were cultured in DMEM containing 10% FBS and 100 U/mL penicillin/streptomycin. HMEC-1 (Human microvascular endothelial cells) were cultured in MCDB131 containing 10% FBS, 10 ng/mL MVGS, and 100 U/mL penicillin/streptomycin. The cells were maintained in a humidified 5% CO_2 incubator at 37 °C. The cells were routinely harvested by treatment with a trypsin−EDTA solution (0.25%).

In Vitro Cytotoxicity Study. The cytotoxicity of the Fe_3O_4@$mSiO_2$, Fe_3O_4@$mSiO_2$−TPP, and Fe_3O_4@$mSiO_2$−TPP/CDs was evaluated using MTT assay with A549, CHO, HeLa, SH-SY5Y, HFF, and HMEC-1 cell lines. Typically, cells were initially seeded in a 96-well cell culture plate at a density of 1×10^4 cells per well for 12 h before different concentrations of the nanoparticle-based samples (50, 100, 200, 300, and 400 μg/mL) were added into each well. After further incubation for 12 or 24 h, the suspension medium was removed and 10 μL MTT (5 mg/mL in PBS solution) was added into each well. After 4 h of incubation, culture supernatants were aspirated and purple formazan crystals were dissolved into 150 mL of DMSO for an additional incubation of 15 min. The concentration of the reduced MTT in each well was measured at a reference wavelength of 630 nm while using a test wavelength of 570 nm employing a microplate reader (318C, INESA Instrument, China). The cell viability was estimated according to the following equation:

$$\text{cell viability (\%)} = \text{OD}_{\text{treated}}/\text{OD}_{\text{control}} \times 100\%$$

in which $OD_{control}$ was obtained in the absence of NPs, and $OD_{treated}$ was obtained in the presence of NPs. The experiments were performed in triplicate. The value of $p < 0.05$ was considered in significance.

Hoechst 33258 Staining. A549, CHO, HeLa, SH-SY5Y, HFF, and HMEC-1 cells from exponentially growing cultures were seeded in 24-well culture plates and each treated with Fe_3O_4@$mSiO_2$, Fe_3O_4@$mSiO_2$−TPP, and Fe_3O_4@$mSiO_2$−TPP/CDs NPs at concentrations of 100 for 24 h, respectively. After coincubation, cells were washed with PBS three times and fixed with 4% paraformaldehyde. Then, cells were stained with 5 μg/mL of Hoechst 33258 for 5 min at room temperature and washed three times with PBS and analyzed under a fluorescent microscope (Olympus IX 51, Japan). The percentage of apoptosis cells (apoptosis rate) in a given sample was determined as the ratio between the number of apoptosis cells in the sample (N_S) and the number of all cells in the same sample (N_{all}): apoptosis rate (%) = $N_S/N_{all} \times 100\%$. The experiments were performed in triplicate. The value of $p < 0.05$ was considered in significance.

Membrane Permeability Assessment. The level of extracellular lactate dehydrogenase (LDH) release was assessed as an indicator of membrane permeability and cytotoxicity. In the LDH assay, cells seeded in a 96-well cell-culture plate at a density of 1×10^4 cells per well were cultured for 24 h. Then, 100 μg/mL Fe_3O_4@$mSiO_2$, Fe_3O_4@$mSiO_2$−TPP, and Fe_3O_4@$mSiO_2$−TPP/CDs NPs were added into different wells, and coincubated with for 3, 6, 12, and 24 h, respectively. The release of the LDH in each sample was determined by measuring the absorbance at a reference wavelength of 630 nm while using a test wavelength of 450 nm with the microplate reader. The results of the LDH assays were expressed as average absorbance values compared to that of untreated control cells. The experiments were performed in triplicate. The value of $p < 0.05$ was considered in significance.

Fluorescent Property of the Fe_3O_4@$mSiO_2$−TPP/CDs Nanoplatform. The multicolor fluorescent imaging of the Fe_3O_4@$mSiO_2$−TPP/CDs-treated cells was excited at three different wavelengths (405, 488, and 559 nm) and observed under the Olympus FV1000 confocal laser scanning microscopy (CLSM). The A549, CHO, HeLa,, SH-SY5Y, HFF, and HMEC-1 cell lines were seeded on a Φ35 mm confocal laser dish at a density of 5×10^4 cells per dish and the medium was changed to the Fe_3O_4@$mSiO_2$−TPP/CDs NPs (100 μg/mL) next day. After further coincubation for 24 h, the cells were washed with PBS three times and fixed with 4% paraformaldehyde.

Mitochondria Colocalization of the Fe_3O_4@$mSiO_2$−TPP/CDs NPs. The HeLa cells were seeded on a Φ35 mm confocal laser dish at a density of 5×10^4 cells per dish. After 12 h, a complete medium containing 100 μg/mL of Fe_3O_4@$mSiO_2$−TPP/CDs was added to the dish, and the cells were incubated for 12 and 24 h, respectively. After being washed two times with PBS, Mitotracker Red (200 nM) or Mitotracker Green (200 nM) was used for staining for 20 min. The cells were then washed twice with PBS, and differential interference contrast (DIC) and fluorescent images were taken with CLSM. In the merged pictures, yellow spots arising from red and green signals and pink spots arising from red and blue signals denote the colocalization of the NPs within mitochondrial compartments.

Mitochondria Colocalization of FITC-labeled Fe_3O_4@$mSiO_2$−TPP NPs. To obtain the FITC-labeled Fe_3O_4@$mSiO_2$−TPP NPs, 2 mg of FITC was dissolved and kept under magnetic stirring in 1.1 mL of absolute ethanol and mixed with 5 μL of APTES for 12 h in the dark. Then, 0.50 mL of FITC/APTES/ethanol solution was added into a round-bottom flask with 0.20 g of the Fe_3O_4@$mSiO_2$−TPP NPs and ethanol solution. The mixture continued stirring for 2 h at 40 °C. The FITC-labeled NPs were collected by centrifuging and washing with ethanol until the supernatant was transparent. The final product was dried under vacuum at 60 °C. As a control, the Fe_3O_4@$mSiO_2$ NPs were labeled by FITC using the same procedure. The A549, CHO, HeLa, SH-SY5Y, HFF, and HMEC-1 cell lines were seeded on confocal laser dishes at a density of 5×10^4 cells per dish and grown overnight in DMEM. The medium was changed and the FITC-labeled Fe_3O_4@$mSiO_2$ and FITC-labeled Fe_3O_4@$mSiO_2$−TPP NPs (100 μg/mL) were added into the dishes to be independently tested. After coincubation for 3, 6, 12, and 24 h, the cells were washed with PBS three times and fixed with 4% paraformaldehyde. Afterward, Mitotracker Red (200 nM) and DAPI (0.80 μg/mL) were added into the cells in sequence, which incubated at 37 °C for 20 min and viewed under a CLSM at room temperature for 5 min. In order to determine the localization of the Fe_3O_4@$mSiO_2$−TPP NPs inside the

DOI: 10.1021/acsami.5b00405
ACS Appl. Mater. Interfaces 2015, 7, 10201−10212

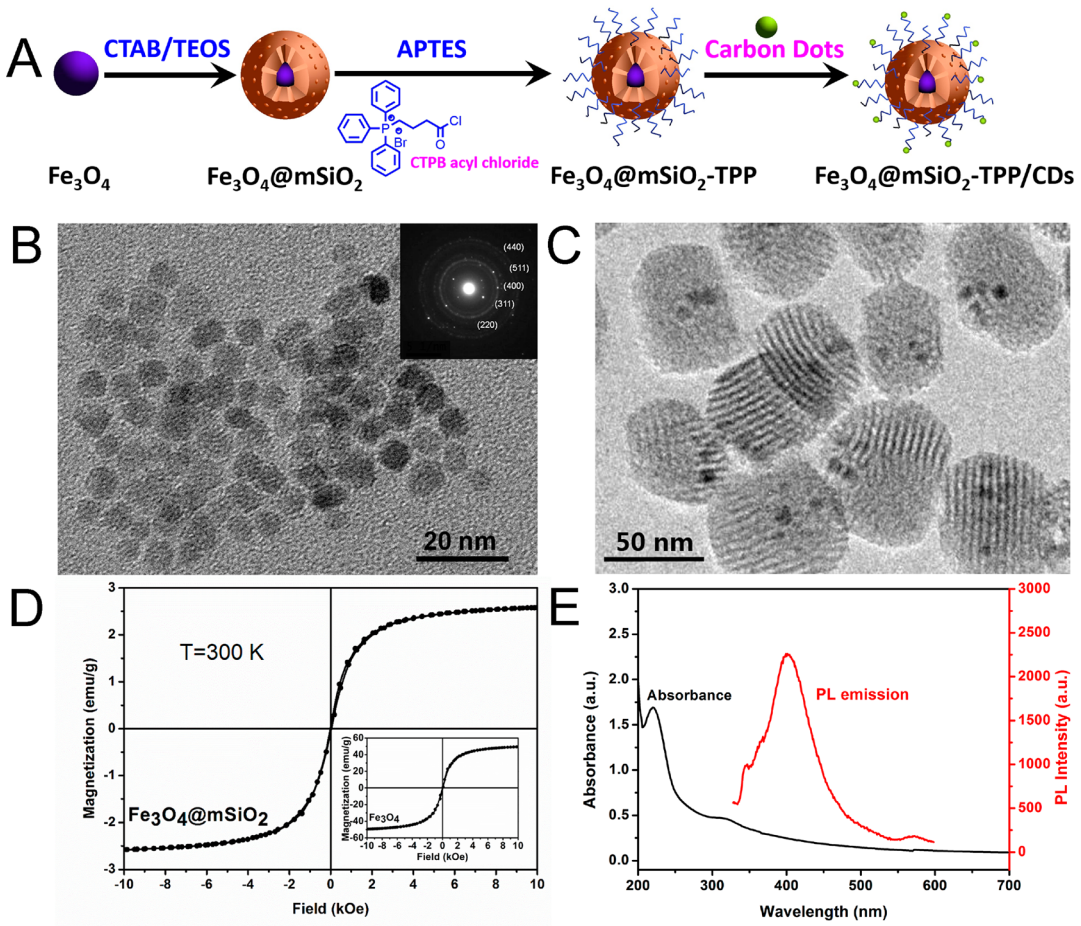

Figure 1. (A) Schematic route of the synthesis of Fe_3O_4@$mSiO_2$−TPP/CDs nanoplatform. (B) Typical TEM image of the Fe_3O_4 NPs (the inset shows the corresponding SAED pattern). (C) Typical TEM image of the Fe_3O_4@$mSiO_2$ NPs. (D) *M*−*H* curve of the Fe_3O_4@$mSiO_2$ NPs at 300 K (the inset shows the *M*−*H* curve of the Fe_3O_4 NPs at 300 K). (E) UV−vis spectrum and PL emission (excited at 310 nm) of the Fe_3O_4@$mSiO_2$−TPP/CDs nanoplatform in ethanol.

mitochondrial compartments, Z-stacked (Z1−17) images of HeLa cells were obtained by capturing serial images of the *x*−*y* planes as hanging the focal length. The upper and the lower surfaces of the cells were selected as the first and last planes. By overlaying fluorescent images of the green fluorescence from the FITC-labeled NPs and the red fluorescence from stained mitochondria, the colocalization of the NPs in mitochondria was indicated as yellow dots.

Lysotracker Red Staining. For Lysotracker Red fluorescent microscopy studies, HeLa cells were plated in a Φ35 mm confocal laser dish at a density of 5×10^4 cells per dish and grown in DMEM. Cells were preincubated for 12 h prior to addition of the testing sample, reaching an approximate confluence of 70%. Cells were then treated with 100 μg/mL of Fe_3O_4@$mSiO_2$−TPP NPs for 12 and 24 h, respectively, followed by staining with Lysotracker Red (250 nM in media) for 30 min and then with DAPI (0.80 μg/mL) nuclear stain for 5 min. Cells were washed twice with PBS to remove free dyes and then observed using the Olympus IX 51 fluorescent microscope.

Flow Cytometry Analysis. The A549, CHO, HeLa, and SH-SY5Y cells were seeded in a 12-well cell culture plate at a density of 2×10^5 cells per well and further coincubated with the FITC-labeled Fe_3O_4@$mSiO_2$ and Fe_3O_4@$mSiO_2$−TPP NPs (100 μg/mL) for 24 h. After being washed three times with PBS, the cells were harvested and suspended in PBS buffer again. The extracellular fluorescence was quenched by resuspending the cells in trypan blue (200 μg/mL) and incubating them for 10 min at room temperature. After washing once again with PBS, the cells were resuspended in PBS and analyzed with a flow cytometer (FACS Calibur, Becton−Dickinson, USA). The collected data were analyzed using the FlowJo software. Cells incubated without the NPs were used as a control.

Cellular Uptake under an Applied Static Magnetic Field. The cellular uptake of the Fe_3O_4@$mSiO_2$−TPP/CDs was performed under a magnetic field, and observed under the CLSM using excitation at 405 nm. After seeded on Φ35 mm confocal laser dishes overnight, HeLa and A549 cells were coincubated with 200 μg/mL of CDs for 1 h and then added in an extra 1 mL of DMEM and 100 μg/mL of Fe_3O_4@$mSiO_2$−TPP NPs for further coincubation in the presence or absence of a static magnetic field (0.30 T), respectively. After coincubation for another 1 h, cells were washed by PBS and fixed with 4% paraformaldehyde for CLSM observations.

As a control, FITC-labeled Fe_3O_4@$mSiO_2$−TPP NPs were also used in follow-up experiments. The A549, CHO, HeLa, SH-SY5Y, HFF, and HMEC-1 cell lines were seeded in Φ35 mm confocal laser dishes at a density of 5×10^4 cells per dish and grown for 24 h in DMEM. Then, the four cell lines were treated with 50 μg/mL FITC-labeled Fe_3O_4@$mSiO_2$−TPP NPs for 0.5, 1, and 3 h, respectively, under a magnetic field by positioning the laser dishes on top of 0.30 T NdFeB permanent magnets. After the coincubation, the cells were fixed with 4% paraformaldehyde and then the nucleus was stained by DAPI (0.80 μg/mL) for microscope viewing. For flow cytometry analysis, the four cell lines were cultivated in a 12-well plate and treated with 50 μg/mL FITC-labeled Fe_3O_4@$mSiO_2$−TPP NPs for 0.5, 1, and 3 h under the applied static magnetic field, respectively. After coincubation, cells were washed to make sure the extracellular fluorescence was quenched while the intracellular fluorescence remained.

Bio-TEM Observations of Cellular Uptake under a Magnetic Field. HeLa cells were seeded in Φ100 mm dishes at a density of 1×10^6 cells per dish. After cultured for 24 h, the HeLa cells were treated

DOI: 10.1021/acsami.5b00405
ACS Appl. Mater. Interfaces 2015, 7, 10201−10212

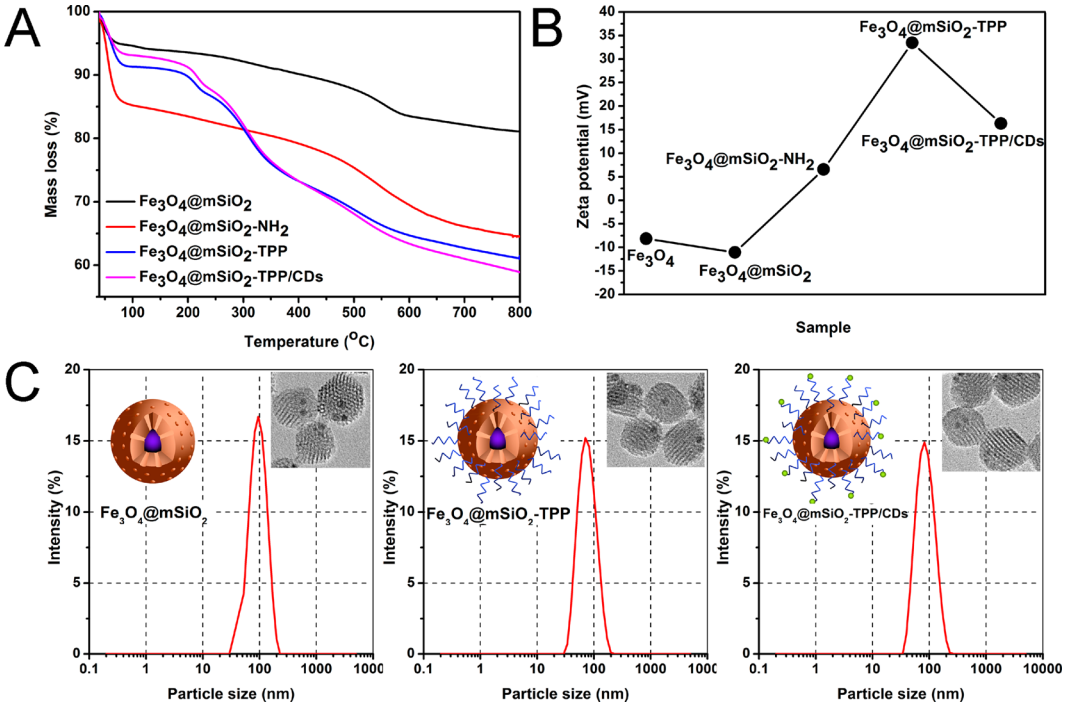

Figure 2. (A) TGA curves, (B) ζ-potentials, and (C) hydrodynamic diameters distribution of the Fe_3O_4@$mSiO_2$, Fe_3O_4@$mSiO_2$−NH_2, Fe_3O_4@$mSiO_2$−TPP, and Fe_3O_4@$mSiO_2$−TPP/CDs NPs (the insets are corresponding TEM images of the NPs with a scale bar of 25 nm).

with the Fe_3O_4@$mSiO_2$−TPP/CDs for 1 h in the presence or absence of an external magnetic field, respectively. For TEM studies, the excess medium of each dish was removed and the cells were washed with PBS solution, trypsined and centrifuged at 5000 rpm for 5 min. Then, the cell pellets were fixed with 2.5% glutaraldehyde for 4 h and postfixed with 1% aqueous osmium tetroxide. The cells were dehydrated through ethanol series and embedded in Epon Araldite resin. Ultrathin sections of 70 nm containing the cells were placed on the grids and double contrasted with 4% uranyl acetate (1:1, acetone:water) and 0.2% Reynolds lead citrate (water), air-dried, and imaged under the 100 kV JEOL-1230 TEM instrument.

RESULT AND DISCUSSION

Morphology and Microstructure of the Fe_3O_4@$mSiO_2$−TPP/CDs Nanoplatform. Figure 1A illustrates the synthesis route of the Fe_3O_4@$mSiO_2$−TPP/CDs nanoplatform in detail. The corresponding TEM images in Figure 1B,C show the as-synthesized Fe_3O_4 NPs and Fe_3O_4@$mSiO_2$ NPs, respectively. The quasi-spherical Fe_3O_4 NPs with an average

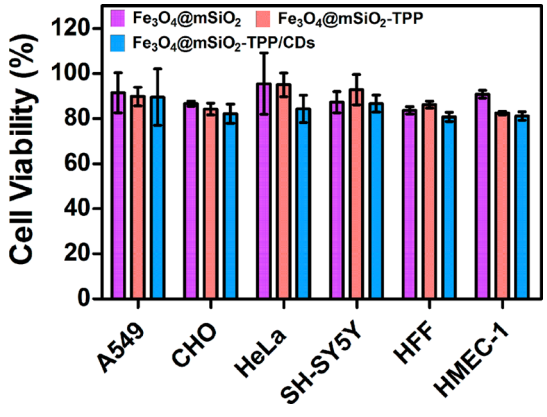

Figure 3. MTT results of A549, CHO, HeLa, SH-SY5Y, HFF, and HMEC-1 cell viabilities after coincubation with the Fe_3O_4@$mSiO_2$, Fe_3O_4@$mSiO_2$−TPP, and Fe_3O_4@$mSiO_2$−TPP/CDs NPs for 24 h at the concentrations of 100 μg/mL. Data are expressed as mean ± SD from three independent experiments ($*p < 0.05$).

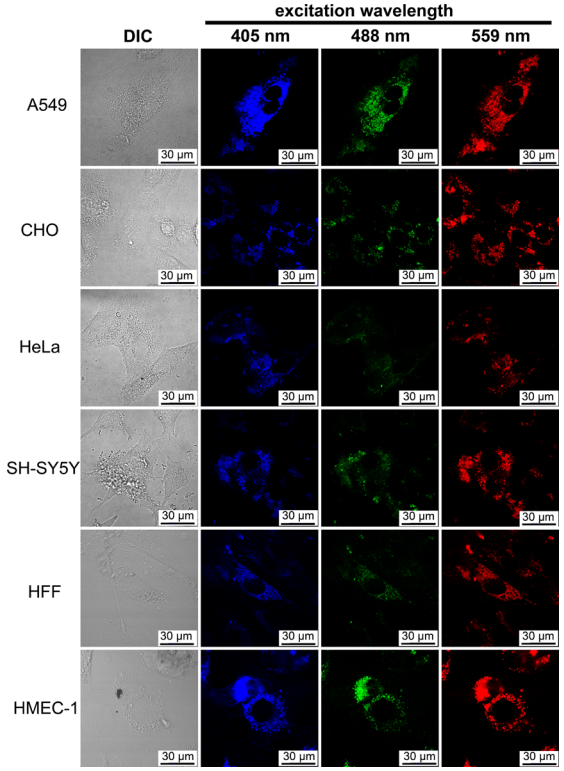

Figure 4. DIC and CLSM images of the A549, CHO, HeLa, SH-SY5Y, HFF, and HMEC-1 cell lines treated with 100 μg/mL of the Fe_3O_4@$mSiO_2$−TPP/CDs for 24 h. The blue, green, and red emissions were excited by 405, 488, and 559 nm laser pulses, respectively.

DOI: 10.1021/acsami.5b00405
ACS Appl. Mater. Interfaces 2015, 7, 10201−10212

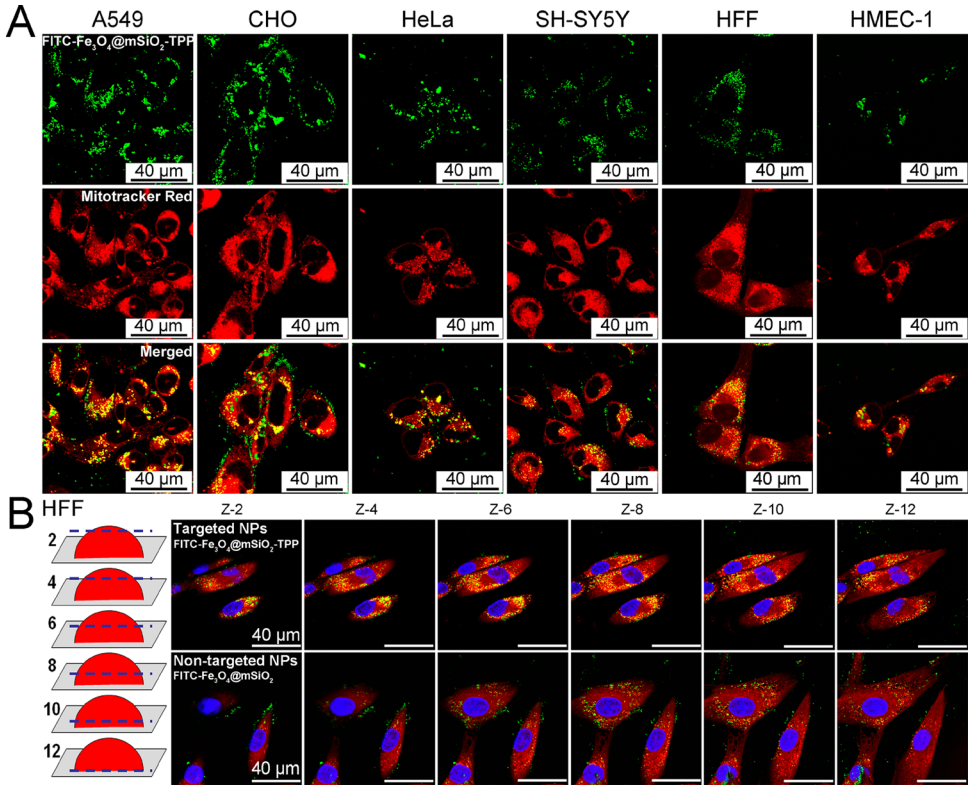

Figure 5. (A) CLSM images of the A549, CHO, HeLa, SH-SY5Y, HFF, and HMEC-1 cell lines exposed to 100 μg/mL of Fe_3O_4@$mSiO_2$−TPP for 24 h. The cells were treated with Mitotracker Red for mitochondrial staining, viewed in the green channel for FITC (ex. 488 nm, em. 519 nm) as while in the red channel for Mitotracker Red (ex. 559 nm, em. 598 nm). Yellow spots arising from the merged red and green signals indicate mitochondrial colocalization of NPs. The scale bar represents 40 μm. (B) CLSM Z-stacked images of the HFF cells exposed to 100 μg/mL of Fe_3O_4@$mSiO_2$−TPP NPs (upper panel) and Fe_3O_4@$mSiO_2$ NPs (lower panel) for 24 h, respectively.

diameter of 6.7 nm were stabilized with hydrophobic oleic acid ligands and well dispersed in *n*-hexane. The narrow size distribution is shown in Figure S1A of the Supporting Information. The selected area electron diffraction (SAED) pattern (see inset of Figure 1B) indicates that the Fe_3O_4 NPs match the cubic magnetite phase (Fe_3O_4, JCPDS No. 72-2303), which agrees well with the XRD pattern as shown in Figure S2A of the Supporting Information. During the preparation of Fe_3O_4@$mSiO_2$ NPs, CTAB was not only used as a stabilizing surfactant for the transfer of the hydrophobic-coated Fe_3O_4 NPs to the aqueous phase[50] but also as a soft template for the mesoporous silica formation.[13] Using this conventional approach, the Fe_3O_4@$mSiO_2$ NPs with an average size of 43.30 nm were successfully prepared as shown in Figure 1C (the size distribution histogram is given in Figure S1B of the Supporting Information). Moreover, Figure S2A of the Supporting Information shows a broad XRD peak in the range of 20°−30° and a narrow peak at 2θ = 35° attributed to the amorphous phase of the mesoporous silica shell and the (311) crystal plane of the Fe_3O_4 core, respectively.[51] Magnetic hysteresis curves in Figure 1D indicate that both Fe_3O_4 and Fe_3O_4@$mSiO_2$ NPs are superparamagnetic at room temperature, which is a desirable property for magnetic separation, targeted drug delivery, MHT, and other applications. Because superparamagnetic NPs can be magnetized under an external magnetic field, however, when the magnetic fluid is removed out from a magnetic field, its bulk magnetization relaxes back to zero, due to the thermal-assisted relaxation processes. Subsequently, the excess of CTAB within the mesoporous silica shell was removed by an ion-exchange procedure using ammonium nitrate.[52] The SAXD pattern of the Fe_3O_4@$mSiO_2$ NPs (Figure S2B of the Supporting Information) displays three peaks corresponding to (100), (110), and (200) planes of a typical two-dimensional hexagonal porous structured MCM-41 material.[53] Moreover, as shown in Figure S2C of the Supporting Information, the N_2 adsorption/desorption isotherms of the Fe_3O_4@$mSiO_2$ NPs can be classified as a type IV isotherm according to the IUPAC nomenclature. The BET surface area and the average pore size of the Fe_3O_4@$mSiO_2$ NPs were calculated to be 1024.42 m^2/g and 5.21 nm, respectively. Figure 1E shows UV−vis absorbance and PL emission (excited at 310 nm) of the Fe_3O_4@$mSiO_2$−TPP/CDs nanoplatform in ethanol.

TPP, a mitochondria-targeting group, is introduced at the surface of the Fe_3O_4@$mSiO_2$ NPs by a nucleophilic substitution reaction of CTPB acyl chloride with the Fe_3O_4@$mSiO_2$−NH_2 NPs, as depicted in Figure 1A. The intermediates and product have been investigated by using ^{1}H NMR spectroscopy, ζ-potential, and TGA. The ^{1}H NMR spectra shown in Figure S3 of the Supporting Information indicate that the CTPB has been synthesized and successfully linked to NH_2-modified $mSiO_2$. According to the TGA curves shown in Figure 2A, the contents of NH_2 groups, TPP, and CDs on the surface of Fe_3O_4@$mSiO_2$ NPs are calculated to be about 19.09%, 12.18%, and 1.76%, respectively. In addition, Figure 2B shows that the Fe_3O_4 NPs exhibits a negative ζ-potential due to the oleic acid-coating, and the Fe_3O_4@$mSiO_2$ NPs also display a negative potential because of the surface silanol groups. However, the ζ-potential shifts from negative to positive after NH_2-group grafting onto the surface of the Fe_3O_4@$mSiO_2$

DOI: 10.1021/acsami.5b00405
ACS Appl. Mater. Interfaces 2015, 7, 10201−10212

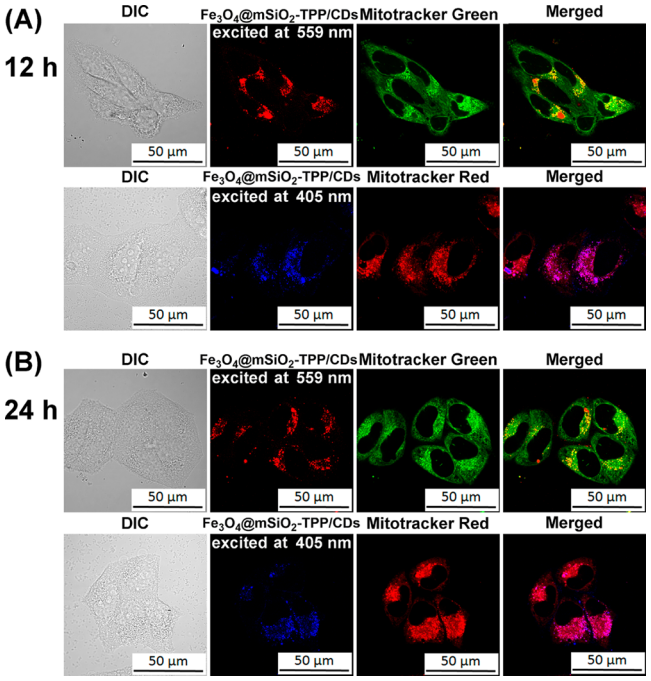

Figure 6. DIC and CLSM images of the HeLa cells exposed to 100 μg/mL of Fe_3O_4@$mSiO_2$−TPP/CDs for (A) 12 h and (B) 24 h. The Fe_3O_4@$mSiO_2$−TPP/CDs NPs were excited at 599 and 405 nm to exhibit red and blue fluorescence, respectively. The cells were treated with Mitotracker Green as well as Mitotracker Red for mitochondrial staining. Yellow spots arising from red and green signals and pink spots arising from red and blue signals denote the colocalization of the NPs within mitochondrial compartments.

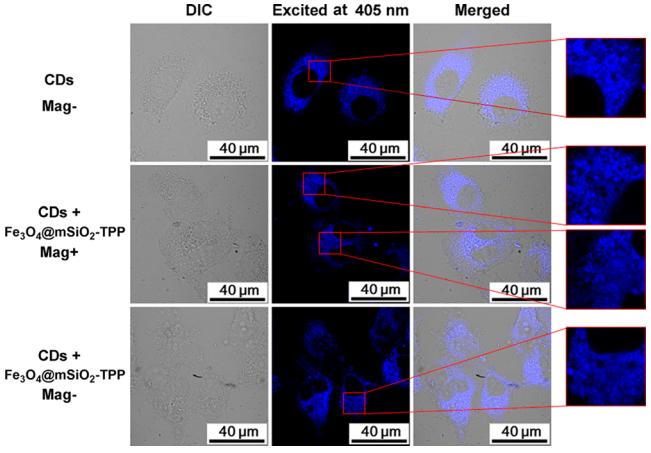

Figure 7. DIC and CLSM images (ex. 405 nm) of the HeLa cells coincubated with 200 μg/mL of CDs for 1 h (upper panel) and then added more DMEM containing 100 μg/mL of Fe_3O_4@$mSiO_2$−TPP NPs to coincubate for one more hour under Mag+ (middle panel) or Mag− (lower panel). The red squares are magnified images of local components in cytoplasm.

NPs. Moreover, it increases abruptly to 33.47 mV after the TPP modification, which confirms the results obtained from ^{1}H NMR and TGA. Figure 2C demonstrates the hydrodynamic sizes of the Fe_3O_4@$mSiO_2$, Fe_3O_4@$mSiO_2$−TPP and Fe_3O_4@$mSiO_2$−TPP/CDs NPs in distilled water changed from 96.82 nm to 73.92 and 82.30 nm, respectively. It is noteworthy that the average size of NPs decreased from 96.82 to 73.92 nm after TPP modification possibly because of the improved dispersity of the TPP-modified NPs. This result is consistent with the ζ-potential data because the particles are more likely to remain dispersed if the absolute value of ζ-potential is higher than 30 mV.[54] The TEM images in the insets of Figure 2C confirm that the Fe_3O_4@$mSiO_2$−TPP NPs have a uniform shape along with a better dispersity. Nevertheless, the average size of Fe_3O_4@$mSiO_2$−TPP NPs has increased a little after conjugation with CDs, but is still less than that of Fe_3O_4@$mSiO_2$ NPs. In the meantime, the ζ-potential of the Fe_3O_4@$mSiO_2$−TPP NPs decreases to +16.33 mV because the CDs own negative ζ-potential of −21.76 mV (not shown here) accounted for a plenty of oxygen-containing groups on the surface of CDs.[55] Both results demonstrate that CDs have conjugated Fe_3O_4@$mSiO_2$−TPP NPs successfully.

In Vitro Cytotoxicity of the Fe_3O_4@$mSiO_2$−TPP/CDs Nanoplatform. Figure 3 shows the MTT result of cell viabilities of A549, CHO, HeLa, SH-SY5Y, HFF, and HMEC-1 cell lines upon treatment with Fe_3O_4@$mSiO_2$, Fe_3O_4@$mSiO_2$−TPP, and Fe_3O_4@$mSiO_2$−TPP/CDs NPs for 12 and 24 h, respectively. The results coming from different cell lines are similar, that is to say, all of the three kinds of NPs induced no significant cytotoxic effect within 24 h at the concentration of 100 μg/mL. Compared to the pristine CDs[47] or reported N-doped CDs,[46] The hybrid nanoplatform shows a higher cytotoxicity mainly because of conjugation with aromatic TPP.[55] Moreover, dose- and time-dependent cytotoxicity profiles for all of the three kinds of NPs are shown in Figure S4 of the Supporting Information. With a further increase in administration dose and coincubation time, the cell viabilities declined correspondingly. Notably, it is more toxic to normal cells such as HFF and HMEC-1 than to the other four cell lines when the concentration of NPs is above 200 μg/mL. On the other hand, apoptosis is one of the major pathways in the process of cell death. Identification of apoptotic cells by staining nuclei with Hoechst 33258 is based on the classic characteristics of apoptosis, namely chromatin condensation and fragmentation of nuclear material.[56] As shown in Figure S5 of the Supporting Information, all of the three kinds of NPs did not induce obvious cell apoptosis at the concentration of 100 μg/mL in all of the A549, CHO, HeLa, SH-SY5Y, HFF, and HMEC-1 cell lines. Therefore, 100 μg/mL was selected as an appropriate concentration to be used in the subsequent cell experiments.

Florescence Imaging of the Fe_3O_4@$mSiO_2$−TPP/CDs Nanoplatform. CDs have demonstrated successful use for fluorescence imaging in vitro[44,57] and in vivo,[43,58] taking advantage of their visible excitation and emission wavelengths, fluorescence brightness at the individual dot level, high photostability, and excellent biocompatibility. Previously, low cytotoxicity and intracellular multicolored fluorescence of CDs internalized by HeLa cells have been studied in our lab.[47] The as-prepared CDs are roughly spherical in shape with an average diameter of 1.90 nm (see Figure S6A of the Supporting Information). The PL of the as-synthesized CDs in ethanol becomes stronger with a red-shift emission as the excitation wavelength increases from 400 to 700 nm, as shown in Figure S6B of the Supporting Information. In fact, the employed CDs made from from konjac flour in our lab are nitrogen-doped CDs, and the QY of the CDs can achieve as high as 22% in ethanol.[47] It is reasonable that the CDs are mainly composed of sp^2-hybridized carbon atoms,[59] and they attached to the Fe_3O_4@$mSiO_2$−TPP NPs through π−π conjugation between the sp^2-hybridized carbon atoms of CDs and the benzene rings

DOI: 10.1021/acsami.5b00405
ACS Appl. Mater. Interfaces 2015, 7, 10201−10212

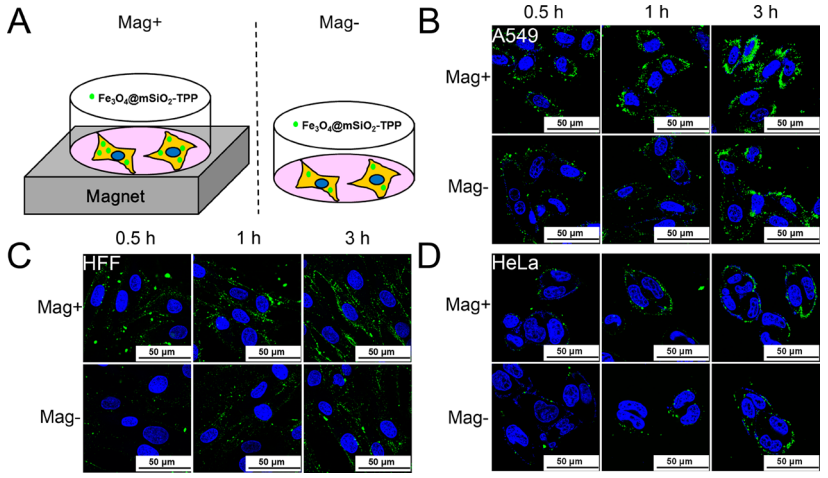

Figure 8. (A) Illustration of the cells exposed to the Fe_3O_4@mSiO$_2$−TPP NPs while positioned or not in a static magnetic field. (B, C, and D) CLSM images of the A549, HFF, and HeLa cell lines treated with 50 μg/mL of the Fe_3O_4@mSiO$_2$−TPP NPs for 0.5, 1, and 3 h under Mag+ or Mag−, respectively. Cell nuclei were stained by DAPI for blue florescence while the green dots around nucleus are the FITC labeled NPs.

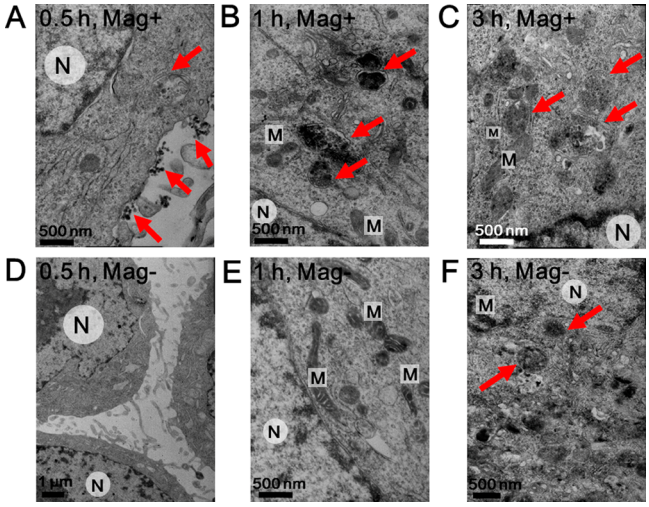

Figure 9. Representative TEM images of the cellular uptake of HeLa cells treated with 100 μg/mL of Fe_3O_4@mSiO$_2$−TPP/CDs (indicated by red arrows) for 0.5, 1, and 3 h in the presence (A, B, and C) or absence (D, E, and F) of a static magnetic field, respectively. "N" represents the nucleus and "M" represents the mitochondria in HeLa cells.

of TPP groups. That is why the QY of the Fe_3O_4@mSiO$_2$−TPP/CDs nanoplatform decreases to 10.07% (estimated by the PL emission, as shown in Figure 1E). Nevertheless, the PL spectra of the CDs, TPP, and TPP/CDs (λ_{ex} = 335 nm) in ethanol are shown in Figure S7A of the Supporting Information, revealing that the PL intensity of the CDs decreases a little after conjugation with TPP, but still exhibits bright blue color under UV lamp at 365 nm (see inset of Figure S7A of the Supporting Information). Figure S7B of the Supporting Information shows PL spectra of TPP/CDs (λ_{ex} = 335 nm) against different exposure times without cells for 0, 0.5, 1, 2, and 3 days, respectively, demonstrating the photostability of the TPP/CDs in cell culture. In addition, we have assessed the impact of other components such as protein BSA and FBS on the fluorescence of the Fe_3O_4@mSiO$_2$−TPP/CDs nanoplatform. As shown in Figure S8 of the Supporting Information, the PL intensity of the nanoplatform increased remarkably in the presence of protein FBS while protein BSA takes no substantial effect on its PL intensity. According to refs 46 and 47, many factors, such as nitrogen-doping and polymer coating on the surface, will have substantial influence on the fluorescence of CDs. In our previous work, the fluorescence of the CDs made in our lab were remarkably increased by polymer (PEG20000) coating on the surface.[47] It is known that protein FBS is an important component in DMEM cell culture, which may be another reason for that the Fe_3O_4@mSiO$_2$−TPP/CDs nanoplatform can keep bright and stable fluorescence when coincubated with different cells lines. Furthermore, the as-constructed Fe_3O_4@mSiO$_2$−TPP/CDs nanoplatform has coincubated with the A549, CHO, HeLa, SH-SY5Y, HFF, and HMEC-1 cell lines for 24 h, respectively. As shown in Figure 4, bright blue, green, and red fluorescence can remain still for as long as 30 min under CLSM while excited by 405, 488, and 559 nm laser pulses, respectively. All of the above-mentioned results indicate that the Fe_3O_4@mSiO$_2$−TPP/CDs nanoplatform is indeed suitable for long time cell imaging.

Mitochondrial Targeting of the Fe_3O_4@mSiO$_2$−TPP/CDs Nanoplatform. First, mitochondrial colocalization of the Fe_3O_4@mSiO$_2$−TPP NPs was studied by using the HeLa cells treated with 100 μg/mL of FITC-labeled Fe_3O_4@mSiO$_2$−TPP NPs for 3, 6, 12, and 24 h, respectively. And nontargeted FITC-labeled Fe_3O_4@mSiO$_2$ NPs were used as a control. Figures S9 and S10 of the Supporting Information show DIC and CLSM images of the HeLa cells after coincubation with the targeted and nontargeted NPs for 3, 6, 12, and 24 h, respectively. Red fluorescence arises from Mitotracker Red-stained mitochondria while green fluorescence comes from FITC-labeled NPs and blue fluorescence comes from the DAPI-dyed nucleus. The appearance of yellow dots from the overlaid red and green channels indicates the colocalization of the mitochondria and the NPs inside the cells. Evidently, an increasing higher degree of colocalization of the FITC-labeled Fe_3O_4@mSiO$_2$−TPP NPs and mitochondrial compartment in the HeLa cells could be found as long as the coincubation time increases from 3 h to 6, 12, and 24 h, respectively, which means a time-dependent mitochondria-targeting behavior of the Fe_3O_4@mSiO$_2$−TPP NPs. On the contrary, fewer yellow dots appeared after the HeLa cells were coincubated with the nontargeted Fe_3O_4@mSiO$_2$ NPs for 24 h. Subsequently, A549, CHO, SH-SY5Y, HFF, and HMEC-1 cell lines were also treated with 100 μg/mL

DOI: 10.1021/acsami.5b00405
ACS Appl. Mater. Interfaces 2015, 7, 10201−10212

of Fe_3O_4@$mSiO_2$−TPP NPs for 24 h in the same protocol as that for HeLa cells. As shown in Figure 5A, and Figure S11 in the Supporting Information, the most obvious mitochondria-targeting effect of the Fe_3O_4@$mSiO_2$−TPP NPs can be seen in A549 and HFF cell lines. To quantify the intracellular uptake of the Fe_3O_4@$mSiO_2$ and Fe_3O_4@$mSiO_2$−TPP NPs, a flow cytometry was employed. Figure S12 of the Supporting Information gives precise fluorescence quantification by fluorescence-activated cell sorting (FACS), in which the obviously higher fluorescence intensity means much more intracellular uptake of Fe_3O_4@$mSiO_2$−TPP NPs than that of Fe_3O_4@$mSiO_2$ NPs. This result is consistent with that of CLSM. At last, z-stacked images show every slice position of HFF cells loaded with the Fe_3O_4@$mSiO_2$−TPP NPs along the *Z*-axis, as illustrated in left side of Figure 5B. Expressive yellow signals in the z-8 and z-10 (the middle layer of the cells) images in the upper row demonstrate the successful localization of the Fe_3O_4@$mSiO_2$−TPP NPs in the mitochondria.

Furthermore, the possible mitochondria-targeting mechanism of TPP-modified NPs was investigated. Mitochondria consist of outer and inner membranes with the highly negative potential ($\Delta\Psi$ = −150 to −200 mV) of outer membrane and with the proton gradient across the inner membrane. TPP is a polar cationic molecule with high lipophilicity that makes it suitable for penetrating the mitochondrial intermembrane potential barrier and has been used in different mitochondria targeting materials.[34] It has been reported that some NPs, such as MSNs, could escape from the endosomes into the cytoplasm by vesicle breakdown after endocytosis.[12] Figure S13 of the Supporting Information shows the fluorescent micrographs of HeLa cells treated with Fe_3O_4@$mSiO_2$−TPP NPs for 12 and 24 h, respectively. The cells were treated with Lysotracker Red for lysomome staining and viewed in the red channel for Lysotracker Red (ex. 559 nm, em. 598 nm) and the green channel for FITC-labeled NPs (ex. 488 nm, em. 519 nm). Yellow spots in the merged images arising from the colocalization of red and green signals indicate lysosomal colocalization of NPs. Compared with the negatively charged MSNs that have a better endosomal escape ability,[60] TPP-modified Fe_3O_4@$mSiO_2$ NPs need more time as long as 24 h to escape from endosomes and lysosomes because of positive surface charge. Although it was recently reported that a boron−dipyrromethene-based fluorescent probe with two TPP moieties gained an unusual lysosome-targeting capability,[61] and some other research suggested the TPP-conjugated polymer could only adsorb onto the surface or taken up into the membranes of mitochondria,[62] it is evident that in the present experiment, the positively charged Fe_3O_4@$mSiO_2$−TPP NPs enriched around the mitochondria, possibly because the membrane potential is the major driving force which allows the entrance and accumulation of the cationic species into mitochondria rather than cell plasma.[63]

Finally, the mitochondrial targeting of the Fe_3O_4@$mSiO_2$−TPP NPs/CDs nanoplatform has been proved. Figure 6 shows DIC and CLSM images of the HeLa cells coincubated with 100 μg/mL of Fe_3O_4@$mSiO_2$−TPP/CDs for 12 and 24 h, respectively. The merged pink signals from CDs (blue channel) and mitochondria (red channel, stained by Mitotracker Red) indicate that Fe_3O_4@$mSiO_2$−TPP/CDs localized in mitochondrial compartments of HeLa cells. Upon using another mitochondrial dye, Mitotracker Green, a similar merged yellow signals from CDs (red channel) and mitochondria (green channel, stained by Mitotracker Green) could also be observed. Theoretically, the NPs internalization would result in an increase of cytoplasmic membrane permeability and the treated cells should release cytoplasmic LDH and other cytotoxic substances into the medium. As shown in Figure S14 of the Supporting Information, the amount of LDH leakage of HeLa cells treated with the Fe_3O_4@$mSiO_2$−TPP/CDs increased as the coincubation time was increased from 3 h to 6, 12, and 24 h.

Internalized Efficiency under Magnetic Field Using Different Cell Lines. It has been reported that the application of an external magnetic field could facilitate the cellular uptake of magnetic NPs, such as plain magnetic NPs functionalized with cell-penetrating peptides (CPPs)[64] or a magnetite core coated with a mesoporous silica shell.[17] Most of the reports have emphasized that a magnetic field has a significant influence on the cellular uptake only within a short coincubation time.[65,66] In the present experiment, CDs were first coincubated with HeLa cells for 1 h and then Fe_3O_4@$mSiO_2$−TPP NPs were added to coincubate for one more hour. As shown in Figure 7, the internalized CDs were captured by Fe_3O_4@$mSiO_2$−TPP NPs and become weaker fluorescent dots in cells. In the presence of an external magnetic field of 0.30 T, more aggregates of fluorescent dots can be observed compared with that in the absence of a magnetic field. A similar result has been obtained for A549 cell line, as shown in Figure S15 of the Supporting Information. Moreover, the time-dependency of the magnetically enhanced cellular uptake of the FITC labeled Fe_3O_4@$mSiO_2$−TPP NPs in A549, CHO, HeLa, HFF, and SH-SY5Y cell lines are demonstrated by CLSM images and flow cytometry data, as shown in Figure 8, and Figure S16 of the Supporting Information, respectively. Correspondingly, a quantitative analysis of the magnetically enhanced cellular uptake in 0.5, 1, and 3 h according FACS has been done, as shown in Table S1 of the Supporting Information. Besides, using the CHO cell line as another cell model to perform the same protocol, no difference can be seen between cellular uptake after coincubation for 24 h under Mag+ or Mag−, as shown in Figure S17 of the Supporting Information. In a word, we found that the magnetically enhanced cellular uptake is a time-dependent behavior, which is significant within a short coincubation time, such as 0.5 or 1 h. Nevertheless, using the CHO cell line as another cell model to perform the same protocol, no difference can be seen between cellular uptake after coincubation for 24 h under Mag+ or Mag−, as shown in Figure S17 of the Supporting Information. Actually, no difference can be observed between the Mag+ and Mag− scenarios after coincubation for more than 3 h, possibly because the internalization become saturated after a long enough time.

As for the mechanism of enhanced cellular effect during a short time, such as 1 h, it is related to the formation of linear aggregates, chain-like, or even columnar structures of magnetic NPs induced by an applied magnetic field.[15] Actually, the magnetically induced aggregation phenomena associated with magnetic colloids have been extensively studied both experimentally and theoretically.[67,68] All the reported studies reveal a remarkable change in the internal mesoscopic structure of the suspended magnetic units as a function of the initial characteristics of the suspension (e.g., particle volume fraction), time of exposure, and applied field strength. As shown in Figure S18 of the Supporting Information, a slower sedimentation process and more cellular uptake can be observed for the Fe_3O_4@$mSiO_2$−TPP NPs when exposed to an external magnetic field within 10 min. Compared to those negative

DOI: 10.1021/acsami.5b00405
ACS Appl. Mater. Interfaces 2015, 7, 10201−10212

charged Fe_3O_4@$mSiO_2$ NPs, the TPP-modified NPs can reduce and/or prevent the aggregation of NPs induced by the external magnetic field due to positively charged TPP moiety.[69]

Finally, the magnetically enhanced cellular uptake of Fe_3O_4@$mSiO_2$−TPP/CDs nanoplatform in HeLa cells has been confirmed by bio-TEM images. Figure 9 shows the internalization and distribution of Fe_3O_4@$mSiO_2$−TPP/CDs inside the HeLa cells under Mag+ or Mag−. In a short coincubation time of 0.5 h, more NPs stayed in the intercellular space or attached to cell membranes under Mag+ compared to that under Mag−. When the coincubated time increased to 1 and 3 h, the internalized NPs and encapsulated into vesicular or cytosolic compartments of HeLa cells can be observed in Figure 9B,C. As a control, less vesicles containing NPs could be observed in the absence of a magnetic field as shown in Figure 9E,F. The result agrees with those reports on mesoporous silica NPs or microparticles.[70]

CONCLUSION

In summary, a multifunctional bionanoplatform has been fabricated consisting of a TPP-modified Fe_3O_4@$mSiO_2$ NPs in conjugation with CDs. The as-constructed bionanoplatform has low cytotoxicity and apoptosis rates in A549, CHO, HeLa, SH-SY5Y, HFF, and HMEC-1 cell lines. TPP modification could facilitate the cellular uptake of the nanoplatform by helping them to escape from endosomes and lysosomes, and then localize in mitochondria. Besides, the nanoplatform also present a cellular uptake response to an external static magnetic field of 0.30 T, which is indeed a time-dependent behavior, too. Above all, conjugation with CDs endows the nanoplatform intracellular multicolored fluorescence that can remain bright and stable inside cells for a long time. This work provides us an efficient and effective pathway to fabricate a hybrid bionanoplatform for integrating mitochondria-targeting, long time cell imaging, and enhanced cellular uptake.

ASSOCIATED CONTENT

Supporting Information

Details regarding the histograms for the size measurement from TEM images, XRD patterns, SAXD pattern and N_2 adsorption/desorption isotherms of Fe_3O_4@$mSiO_2$ NPs, ^1H NMR spectrum of TPP and NPs, PL emissions of CDs and TPP/CDs, cell viability and apoptosis rate of NPs in different concentrations, CLSM images of HeLa cells coincubated for different time, the histograms of LDH release, fluorescent micrographs of Lysotracker stained, CLSM images of CHO cells treated with NPs for 24 h under a applied magnetic field, TEM image of CDs and cell imaging of Fe_3O_4@$mSiO_2$−TPP/CDs NPs. The Supporting Information is available free of charge on the ACS Publications website at DOI: 10.1021/acsami.5b00405.

AUTHOR INFORMATION

Corresponding Author

*H. Bi. Tel/Fax: +86 551 63861279. E-mail: bihong@ahu.edu.cn.

Notes

The authors declare no competing financial interest.

ACKNOWLEDGMENTS

This work was financed by the 211 Project of Anhui University, the National Natural Science Foundations of China (Grant No. 51272002 and 51403002), Anhui Provincial Natural Science Foundation (1208085ME87), and the Technology Foundation for Selected Overseas Chinese Scholar, Ministry of Personnel of China (No. [2013]-385). We thank the Key Laboratory of Environment-Friendly Polymer Materials of Anhui Province, and Collaborative Innovation Center of Modern Biomanufacture, Anhui University. Additionally, we thank the lab of Professor Xuebiao Yao (School of Life Science, University of Science and Technology of China, China) for providing HeLa cells, and we also thank Associate Professor Hengli Tang (Department of Biological Science, Florida State University, USA) and Professor Mikhail Oshtrakh (Institute of Physics and Technology, Ural Federal University, Russia) for improving the English of the paper. Finally, we are very grateful to Professor Yu Chen (The Institute Biomedical Engineering and Nano Science, School of Medicine of Tongji University, China) for the enthusiastic suggestion on revising the paper.

REFERENCES

(1) Kateb, B.; Chiu, K.; Black, K. L.; Yamamoto, V.; Khalsa, B.; Ljubimova, J. Y.; Ding, H.; Patil, R.; Portilla-Arias, J. A.; Modo, M.; Moore, D. F.; Farahani, K.; Okun, M. S.; Prakash, N.; Neman, J.; Ahdoot, D.; Grundfest, W.; Nikzad, S.; Heiss, J. D. Nanoplatforms for Constructing New Approaches to Cancer Treatment, Imaging, and Drug Delivery: What Should Be the Policy? *NeuroImage* **2011**, *54*, S106−S124.

(2) Topete, A.; Alatorre-Meda, M.; Iglesias, P.; Villar-Alvarez, E. M.; Barbosa, S.; Costoya, J. A.; Taboada, P.; Mosquera, V. Fluorescent Drug-Loaded, Polymeric-based, Branched Gold Nanoshells for Localized Multimodal Therapy and Imaging of Tumoral Cells. *ACS Nano* **2014**, *8*, 2725−2738.

(3) Xu, C. J.; Sun, S. H. New Forms of Superparamagnetic Nanoparticles for Biomedical Applications. *Adv. Drug Delivery Rev.* **2013**, *65*, 732−743.

(4) Kievit, F. M.; Zhang, M. Q. Surface Engineering of Iron Oxide Nanoparticles for Targeted Cancer Therapy. *Acc. Chem. Res.* **2011**, *44*, 853−862.

(5) Jing, L. M.; Ding, K.; Kershaw, S. V.; Kempson, I. M.; Rogach, A. L.; Gao, M. Y. Magnetically Engineered Semiconductor Quantum Dots as Multimodal Imaging Probes. *Adv. Mater.* **2014**, *26*, 6367−6386.

(6) Chen, M. L.; He, Y. J.; Chen, X. W.; Wang, J. H. Quantum Dots Conjugated with Fe_3O_4-Filled Carbon Nanotubes for Cancer-Targeted Imaging and Magnetically Guided Drug Delivery. *Langmuir* **2012**, *28*, 16469−16476.

(7) Zhang, F.; Braun, G. B.; Pallaoro, A.; Zhang, Y.; Shi, Y.; Cui, D.; Moskovits, M.; Zhao, D.; Stucky, G. D. Mesoporous Multifunctional Upconversion Luminescent and Magnetic "Nanorattle" Materials for Targeted Chemotherapy. *Nano Lett.* **2011**, *12*, 61−67.

(8) Li, Z.; Wang, C.; Cheng, L.; Gong, H.; Yin, S.; Gong, Q.; Li, Y.; Liu, Z. PEG-Functionalized Iron Oxide Nanoclusters Loaded with Chlorin E6 for Targeted, NIR Light Induced, Photodynamic Therapy. *Biomaterials* **2013**, *34*, 9160−9170.

(9) Lin, L. S.; Cong, Z. X.; Cao, J. B.; Ke, K. M.; Peng, Q. L.; Gao, J. H.; Yang, H. H.; Liu, G.; Chen, X. Y. Multifunctional Fe_3O_4@Polydopamine Core-Shell Nanocomposites for Intracellular mRNA Detection and Imaging-Guided Photothermal Therapy. *ACS Nano* **2014**, *8*, 3876−3883.

(10) Zhang, J.; Yuan, Z. F.; Wang, Y.; Chen, W. H.; Luo, G. F.; Cheng, S. X.; Zhuo, R. X.; Zhang, X. Z. Multifunctional Envelope-Type Mesoporous Silica Nanoparticles for Tumor-Triggered Targeting Drug Delivery. *J. Am. Chem. Soc.* **2013**, *135*, 5068−5073.

DOI: 10.1021/acsami.5b00405
ACS Appl. Mater. Interfaces 2015, 7, 10201−10212

(11) Li, Z. Y.; Liu, Y.; Wang, X. Q.; Liu, L. H.; Hu, J. J.; Luo, G. F.; Chen, W. H.; Rong, L.; Zhang, X. Z. One-Pot Construction of Functional Mesoporous Silica Nanoparticles for the Tumor-Acidity-Activated Synergistic Chemotherapy of Glioblastoma. *ACS Appl. Mater. Interfaces* **2013**, *5*, 7995−8001.
(12) Li, X. Y.; He, Q. J.; Shi, J. L. Global Gene Expression Analysis of Cellular Death Mechanisms Induced by Mesoporous Silica Nanoparticle-based Drug Delivery System. *ACS Nano* **2014**, *8*, 1309−1320.
(13) Kim, J.; Kim, H. S.; Lee, N.; Kim, T.; Kim, H.; Yu, T.; Song, I. C.; Moon, W. K.; Hyeon, T. Multifunctional Uniform Nanoparticles Composed of a Magnetite Nanocrystal Core and a Mesoporous Silica Shell for Magnetic Resonance and Fluorescence Imaging and for Drug Delivery. *Angew. Chem., Int. Ed.* **2008**, *47*, 8438−8441.
(14) Bakandritsos, A.; Papagiannopoulos, A.; Anagnostou, E. N.; Avgoustakis, K.; Zboril, R.; Pispas, S.; Tucek, J.; Ryukhtin, V.; Bouropoulos, N.; Kolokithas-Ntoukas, A.; Steriotis, T. A.; Keiderling, U.; Winnefeld, F. Merging High Doxorubicin Loading with Pronounced Magnetic Response and Bio-repellent Properties in Hybrid Drug Nanocarriers. *Small* **2012**, *8*, 2381−2393.
(15) Perica, K.; Tu, A.; Richter, A.; Bieler, J. G.; Edidin, M.; Schneck, J. P. Magnetic Field-Induced T Cell Receptor Clustering by Nanoparticles Enhances T Cell Activation and Stimulates Antitumor Activity. *ACS Nano* **2014**, *8*, 2252−2260.
(16) Amendola, V.; Meneghetti, M.; Granozzi, G.; Agnoli, S.; Polizzi, S.; Riello, P.; Boscaini, A.; Anselmi, C.; Fracasso, G.; Colombatti, M.; Innocenti, C.; Gatteschi, D.; Sangregorio, C. Top-Down Synthesis of Multifunctional Iron Oxide Nanoparticles for Macrophage Labelling and Manipulation. *J. Mater. Chem.* **2011**, *21*, 3803−3813.
(17) Liu, Q.; Zhang, J. X.; Xia, W. L.; Gu, H. C. Magnetic Field Enhanced Cell Uptake Efficiency of Magnetic Silica Mesoporous Nanoparticles. *Nanoscale* **2012**, *4*, 3415−3421.
(18) Won, Y.-H.; Aboagye, D.; Jang, H. S.; Jitianu, A.; Stanciu, L. A. Core/Shell Nanoparticles as Hybrid Platforms for the Fabrication of a Hydrogen Peroxide Biosensor. *J. Mater. Chem.* **2010**, *20*, 5030−5034.
(19) Li, Z. H.; Dong, K.; Huang, S.; Ju, E. G.; Liu, Z.; Yin, M. L.; Ren, J. S.; Qu, X. G. A Smart Nanoassembly for Multistage Targeted Drug Delivery and Magnetic Resonance Imaging. *Adv. Funct. Mater.* **2014**, *24*, 3612−3620.
(20) Fulda, S.; Galluzzi, L.; Kroemer, G. Targeting Mitochondria for Cancer Therapy. *Nat. Rev. Drug Discovery* **2010**, *9*, 447−464.
(21) Shah, B. P.; Pasquale, N.; De, G.; Tan, T.; Ma, J.; Lee, K.-B. Core-Shell Nanoparticle-based Peptide Therapeutics and Combined Hyperthermia for Enhanced Cancer Cell Apoptosis. *ACS Nano* **2014**, *8*, 9379−9387.
(22) Biswas, S.; Torchilin, V. P. Nanopreparations for Organelle-Specific Delivery in Cancer. *Adv. Drug Delivery Rev.* **2014**, *66*, 26−41.
(23) Durazo, S. A.; Kompella, U. B. Functionalized Nanosystems for Targeted Mitochondrial Delivery. *Mitochondrion* **2012**, *12*, 190−201.
(24) Edeas, M.; Weissig, V. Targeting Mitochondria: Strategies, Innovations and Challenges the Future of Medicine Will Come through Mitochondria. *Mitochondrion* **2013**, *13*, 389−390.
(25) Jean, S. R.; Tulumello, D. V.; Wisnovsky, S. P.; Lei, E. K.; Pereira, M. P.; Kelley, S. O. Molecular Vehicles for Mitochondrial Chemical Biology and Drug Delivery. *ACS Chem. Biol.* **2014**, *9*, 323−333.
(26) Boddapati, S. V.; Tongcharoensirikul, P.; Hanson, R. N.; D'Souza, G. G.; Torchilin, V. P.; Weissig, V. Mitochondriotropic Liposomes. *J. Liposome Res.* **2005**, *15*, 49−58.
(27) Smith, R. A.; Porteous, C. M.; Gane, A. M.; Murphy, M. P. Delivery of Bioactive Molecules to Mitochondria *in Vivo*. *Proc. Natl. Acad. Sci. U. S. A.* **2003**, *100*, 5407−5412.
(28) James, A. M.; Sharpley, M. S.; Manas, A.-R. B.; Frerman, F. E.; Hirst, J.; Smith, R. A.; Murphy, M. P. Interaction of the Mitochondria-Targeted Antioxidant MitoQ with Phospholipid Bilayers and Ubiquinone Oxidoreductases. *J. Biol. Chem.* **2007**, *282*, 14708−14718.
(29) Boddapati, S. V.; D'Souza, G. G.; Erdogan, S.; Torchilin, V. P.; Weissig, V. Organelle-targeted Nanocarriers: Specific Delivery of Liposomal Ceramide to Mitochondria Enhances its Cytotoxicity *in Vitro* and *in Vivo*. *Nano Lett.* **2008**, *8*, 2559−2563.
(30) Biswas, S.; Dodwadkar, N. S.; Piroyan, A.; Torchilin, V. P. Surface Conjugation of Triphenylphosphonium to Target Poly(amidoamine) Dendrimers to Mitochondria. *Biomaterials* **2012**, *33*, 4773−4782.
(31) Marrache, S.; Dhar, S. Engineering of Blended Nanoparticle Platform for Delivery of Mitochondria-Acting Therapeutics. *Proc. Natl. Acad. Sci. U. S. A.* **2012**, *109*, 16288−16293.
(32) Wang, X. H.; Peng, H. S.; Yang, L.; You, F. T.; Teng, F.; Tang, A. W.; Zhang, F. J.; Li, X. H. Poly-L-lysine Assisted Synthesis of Core-Shell Nanoparticles and Conjugation with Triphenylphosphonium to Target Mitochondria. *J. Mater. Chem. B* **2013**, *1*, 5143−5152.
(33) Marrache, S.; Tundup, S.; Harn, D. A.; Dhar, S. *Ex Vivo* Programming of Dendritic Cells by Mitochondria-Targeted Nanoparticles to Produce Interferon-Gamma for Cancer Immunotherapy. *ACS Nano* **2013**, *7*, 7392−7402.
(34) Chakraborty, A.; Jana, N. R. Design and Synthesis of Triphenylphosphonium Functionalized Nanoparticle Probe for Mitochondria Targeting and Imaging. *J. Phys. Chem. C* **2015**, *119*, 2888−2895.
(35) Liu, B.; Shah, M.; Zhang, G.; Liu, Q.; Pang, Y. Biocompatible Flavone-based Fluorogenic Probes for Quick Wash-Free Mitochondrial Imaging in Living Cells. *ACS Appl. Mater. Interfaces* **2014**, *6*, 21638−21644.
(36) Michalet, X.; Pinaud, F. F.; Bentolila, L. A.; Tsay, J. M.; Doose, S.; Li, J. J.; Sundaresan, G.; Wu, A. M.; Gambhir, S. S.; Weiss, S. Quantum Dots for Live Cells, *in Vivo* Imaging, and Diagnostics. *Science* **2005**, *307*, 538−544.
(37) Chen, N.; He, Y.; Su, Y. Y.; Li, Y. M.; Huang, Q.; Wang, H. F.; Zhang, X. Z.; Tai, R. Z.; Fan, C. H. The Cytotoxicity of Cadmium-based Quantum Dots. *Biomaterials* **2012**, *33*, 1238−1244.
(38) Cao, L.; Wang, X.; Meziani, M. J.; Lu, F.; Wang, H.; Luo, P. G.; Lin, Y.; Harruff, B. A.; Veca, L. M.; Murray, D.; Xie, S. Y.; Sun, Y. P. Carbon Dots for Multiphoton Bioimaging. *J. Am. Chem. Soc.* **2007**, *129*, 11318−11319.
(39) He, Y.; Su, Y. Y.; Yang, X. B.; Kang, Z. H.; Xu, T. T.; Zhang, R. Q.; Fan, C. H.; Lee, S. T. Photo and pH Stable, Highly-Luminescent Silicon Nanospheres and Their Bioconjugates for Immunofluorescent Cell Imaging. *J. Am. Chem. Soc.* **2009**, *131*, 4434−4438.
(40) Chen, X. X.; Jin, Q. Q.; Wu, L. Z.; Tung, C. H.; Tang, X. J. Synthesis and Unique Photoluminescence Properties of Nitrogen-Rich Quantum Dots and Their Applications. *Angew. Chem., Int. Ed.* **2014**, *53*, 12542−12547.
(41) Sun, Y. P.; Zhou, B.; Lin, Y.; Wang, W.; Fernando, K. A. S.; Pathak, P.; Meziani, M. J.; Harruff, B. A.; Wang, X.; Wang, H. F.; Luo, PJ. G.; Yang, H.; Kose, M. E.; Chen, B. L.; Veca, L. M.; Xie, S. Y. Quantum-Sized Carbon Dots for Bright and Colorful Photoluminescence. *J. Am. Chem. Soc.* **2006**, *128*, 7756−7757.
(42) Xu, X. Y.; Ray, R.; Gu, Y. L.; Ploehn, H. J.; Gearheart, L.; Raker, K.; Scrivens, W. A. Electrophoretic Analysis and Purification of Fluorescent Single-Walled Carbon Nanotube Fragments. *J. Am. Chem. Soc.* **2004**, *126*, 12736−12737.
(43) Yang, S. T.; Cao, L.; Luo, P. G. J.; Lu, F. S.; Wang, X.; Wang, H. F.; Meziani, M. J.; Liu, Y. F.; Qi, G.; Sun, Y. P. Carbon Dots for Optical Imaging *in Vivo*. *J. Am. Chem. Soc.* **2009**, *131*, 11308−11309.
(44) Luo, P. J. G.; Sahu, S.; Yang, S. T.; Sonkar, S. K.; Wang, J. P.; Wang, H. F.; LeCroy, G. E.; Cao, L.; Sun, Y. P. Carbon "Quantum" Dots for Optical Bioimaging. *J. Mater. Chem. B* **2013**, *1*, 2116−2127.
(45) Dong, Y. Q.; Pang, H. C.; Yang, H. B.; Guo, C. X.; Shao, J. W.; Chi, Y. W.; Li, C. M.; Yu, T. Carbon-based Dots Co-doped with Nitrogen and Sulfur for High Quantum Yield and Excitation-Independent Emission. *Angew. Chem., Int. Ed.* **2013**, *52*, 7800−7804.
(46) Qian, Z. S.; Ma, J. J.; Shan, X. Y.; Feng, H.; Shao, L. X.; Chen, J. R. Highly Luminescent N-Doped Carbon Quantum Dots as an Effective Multifunctional Fluorescence Sensing Platform. *Chem.—Eur. J.* **2014**, *20*, 2254−2263.
(47) Teng, X. Y.; Ma, C. G.; Ge, C. J.; Yan, M. Q.; Yang, J. X.; Zhang, Y.; Morais, P. C.; Bi, H. Green Synthesis of Nitrogen-Doped Carbon Dots from Konjac Flour with "off-on" Fluorescence by Fe^{3+} and L-lysine for Bioimaging. *J. Mater. Chem. B* **2014**, *2*, 4631−4639.

DOI: 10.1021/acsami.5b00405
ACS Appl. Mater. Interfaces 2015, 7, 10201−10212

(48) Liang, X.; Wang, X.; Zhuang, J.; Chen, Y. T.; Wang, D. S.; Li, Y. D. Synthesis of Nearly Monodisperse Iron Oxide and Oxyhydroxide Nanocrystals. *Adv. Funct. Mater.* **2006**, *16*, 1805−1813.
(49) Liong, M.; Lu, J.; Kovochich, M.; Xia, T.; Ruehm, S. G.; Nel, A. E.; Tamanoi, F.; Zink, J. I. Multifunctional Inorganic Nanoparticles for Imaging, Targeting, and Drug Delivery. *ACS Nano* **2008**, *2*, 889−896.
(50) Fan, H.; Yang, K.; Boye, D. M.; Sigmon, T.; Malloy, K. J.; Xu, H.; López, G. P.; Brinker, C. J. Self-Assembly of Ordered, Robust, Three-Dimensional Gold Nanocrystal/Silica Arrays. *Science* **2004**, *304*, 567−571.
(51) Wang, Y. J.; Peng, X. H.; Shi, J. M.; Tang, X. L.; Jiang, J.; Liu, W. S. Highly Selective Fluorescent Chemosensor for Zn^{2+} Derived from Inorganic-Organic Hybrid Magnetic Core/Shell Fe_3O_4@SiO_2 Nanoparticles. *Nanoscale Res. Lett.* **2012**, *7*, 1−13.
(52) Lang, N.; Tuel, A. A Fast and Efficient Ion-Exchange Procedure to Remove Surfactant Molecules from MCM-41 Materials. *Chem. Mater.* **2004**, *16*, 1961−1966.
(53) Grün, M.; Lauer, I.; Unger, K. K. The Synthesis of Micrometer- and Submicrometer-Size Spheres of Ordered Mesoporous Oxide MCM-41. *Adv. Mater.* **1997**, *9*, 254−257.
(54) Jiang, J.; Oberdörster, G.; Biswas, P. Characterization of Size, Surface Charge, and Agglomeration State of Nanoparticle Dispersions for Toxicological Studies. *J. Nanopart. Res.* **2009**, *11*, 77−89.
(55) Wang, B. B.; Wang, Y. F.; Wu, H.; Song, X. J.; Guo, X.; Zhang, D. M.; Ma, X. J.; Tan, M. Q. A Mitochondria-targeted Fluorescent Probe Based on TPP-Conjugated Carbon Dots for Both One- and Two-Photon Fluorescence Cell Imaging. *RSC Adv.* **2014**, *4*, 49960−49963.
(56) Villanueva, A.; De La Presa, P.; Alonso, J.; Rueda, T.; Martinez, A.; Crespo, P.; Morales, M.; Gonzalez-Fernandez, M.; Valdes, J.; Rivero, G. Hyperthermia HeLa Cell Treatment with Silica-Coated Manganese Oxide Nanoparticles. *J. Phys. Chem. C* **2010**, *114*, 1976−1981.
(57) Wu, Z. L.; Zhang, P.; Gao, M. X.; Liu, C. F.; Wang, W.; Leng, F.; Huang, C. Z. One-pot Hydrothermal Synthesis of Highly Luminescent Nitrogen-Doped Amphoteric Carbon Dots for Bioimaging from Bombyx Mori Silk-Natural Proteins. *J. Mater. Chem. B* **2013**, *1*, 2868−2873.
(58) Huang, X. L.; Zhang, F.; Zhu, L.; Choi, K. Y.; Guo, N.; Guo, J. X.; Tackett, K.; Anilkumar, P.; Liu, G.; Quan, Q. M.; Choi, H. S.; Niu, G.; Sun, Y. P.; Lee, S.; Chen, X. Y. Effect of Injection Routes on the Biodistribution, Clearance, and Tumor Uptake of Carbon Dots. *ACS Nano* **2013**, *7*, 5684−5693.
(59) Wang, X.; Cao, L.; Lu, F.; Meziani, M. J.; Li, H.; Qi, G.; Zhou, B.; Harruff, B. A.; Kermarrec, F.; Sun, Y. P. Photoinduced Electron Transfers with Carbon Dots. *Chem. Commun.* **2009**, *25*, 3774−3776.
(60) Slowing, I.; Trewyn, B. G.; Lin, V. S. Effect of Surface Functionalization of MCM-41-Type Mesoporous Silica Nanoparticles on the Endocytosis by Human Cancer Cells. *J. Am. Chem. Soc.* **2006**, *128*, 14792−14793.
(61) Zhang, X. F.; Wang, C.; Han, Z.; Xiao, Y. A Photostable near-Infrared Fluorescent Tracker with pH Independent Specificity to Lysosomes for Long Time and Multicolor Imaging. *ACS Appl. Mater. Interfaces* **2014**, *6*, 21669−21676.
(62) Breunig, M.; Bauer, S.; Goefferich, A. Polymers and Nanoparticles: Intelligent Tools for Intracellular Targeting? *Eur. J. Pharm. Biopharm.* **2008**, *68*, 112−128.
(63) Hoye, A. T.; Davoren, J. E.; Wipf, P.; Fink, M. P.; Kagan, V. E. Targeting Mitochondria. *Acc. Chem. Res.* **2008**, *41*, 87−97.
(64) Smith, C.-A. M.; Fuente, J. d. l.; Pelaz, B.; Furlani, E. P.; Mullin, M.; Berry, C. C. The Effect of Static Magnetic Fields and Tat Peptides on Cellular and Nuclear Uptake of Magnetic Nanoparticles. *Biomaterials* **2010**, *31*, 4392−4400.
(65) Shah, B.; Yin, P. T.; Ghoshal, S.; Lee, K. B. Multimodal Magnetic Core-Shell Nanoparticles for Effective Stem-Cell Differentiation and Imaging. *Angew. Chem., Int. Ed.* **2013**, *52*, 6190−6195.
(66) Lu, Y. C.; Luo, P. C.; Huang, C. W.; Leu, Y. L.; Wang, T. H.; Wei, K. C.; Wang, H. E.; Ma, Y. H. Augmented Cellular Uptake of Nanoparticles Using Tea Catechins: Effect of Surface Modification on Nanoparticle-Cell Interaction. *Nanoscale* **2014**, *6*, 10297−10306.
(67) Faraudo, J.; Andreu, J. S.; Camacho, J. Understanding Diluted Dispersions of Superparamagnetic Particles under Strong Magnetic Fields: A Review of Concepts, Theory and Simulations. *Soft Matter* **2013**, *9*, 6654−6664.
(68) Saville, S. L.; Woodward, R. C.; House, M. J.; Tokarev, A.; Hammers, J.; Qi, B.; Shaw, J.; Saunders, M.; Varsani, R. R.; Pierre, T. G., St; Mefford, O. T. The Effect of Magnetically Induced Linear Aggregates on Proton Transverse Relaxation Rates of Aqueous Suspensions of Polymer Coated Magnetic Nanoparticles. *Nanoscale* **2013**, *5*, 2152−2163.
(69) Gulin Sarfraz, T.; Zhang, J.; Desai, D.; Teuho, J.; Sarfraz, J.; Jiang, H.; Zhang, C.; Sahlgren, C.; Lindén, M.; Gu, H. Combination of Magnetic Field and Surface Functionalization for Reaching Synergistic Effects in Cellular Labeling by Magnetic Core-Shell Nanospheres. *Biomater. Sci.* **2014**, *2*, 1750−1760.
(70) Tao, Z. M.; Toms, B.; Goodisman, J.; Asefa, T. Mesoporous Silica Microparticles Enhance the Cytotoxicity of Anticancer Platinum Drugs. *ACS Nano* **2010**, *4*, 789−794.

DOI: 10.1021/acsami.5b00405
ACS Appl. Mater. Interfaces 2015, 7, 10201−10212